Title	Effects of heat accumulation strategies on defects and microstructure of pure chromium fabricated by laser powder bed fusion: An experimental and numerical study
Author(s)	Park, Sung Hyun; Gokcekaya, Ozkan; Nitomakida, Tatsuya et al.
Citation	Journal of Materials Research and Technology. 2024, 33, p. 7333-7344
Version Type	VoR
URL	https://hdl.handle.net/11094/99694
rights	This article is licensed under a Creative Commons Attribution 4.0 International License.
Note	

Effects of heat accumulation strategies on defects and microstructure of pure chromium fabricated by laser powder bed fusion: An experimental and numerical study

Sung-Hyun Park [a], Ozkan Gokcekaya [a,b,*], Tatsuya Nitomakida [a], Takayoshi Nakano [a,b,**]

[a] Division of Materials and Manufacturing Science, Graduate School of Engineering, Osaka University, 2-1 Yamadaoka, Suita, Osaka, 565-0871, Japan
[b] Anisotropic Design and Additive Manufacturing Research Center, Osaka University, 2-1 Yamadaoka, Suita, Osaka, 565-0871, Japan

ARTICLE INFO

ABSTRACT

The process of employing laser powder bed fusion (L-PBF) process to refractory materials, such as chromium (Cr), remains challenging because of its high ductile-brittle transition temperature. Therefore, a strategy is required to increase the processing temperature to prevent defects. The focus of this study is to clarify the effect of the preheat temperature and scan length variations on defects during the L-PBF process with an experimental and numerical study. Applying a high preheat temperature and short scan length was effective in mitigating the defects. By tuning the heat accumulation strategies, the determined relative density measured by the Archimedes principle and optical measurement of pure Cr parts increased from 97.2% to 99.8% and 97.4% to 99.2%, respectively. The numerical study indicated that deepened and elongated melt pool geometry owing to heat accumulation promoted epitaxial growth. Strong crystallographic texture formation with epitaxial growth led to higher grain size, lower high-angle grain boundary misorientation, Kernel average misorientation, and Taylor factor, which resulted in densification by preventing defects. The hardness of L-PBFed Cr samples gradually decreased with the stronger crystallographic texture formation and compressive yield strength exhibited the same phenomenon. However, the high densification sample with strong crystallographic texture promised the highest compressive strength and strain because it allows single and multi-slip operation during the compressive deformation without premature fracture. This study is a pivotal moment in heat accumulation strategies to achieve high densification for brittle materials fabricated by the L-PBF process while proposing an approach to ensure the reliability of structural applications.

1. Introduction

Recently, novel high-temperature structural materials have been required to develop for industrial applications such as energy conversion systems and aerospace industries, the refractory metal chromium (Cr) and its alloys have been explored for several decades as candidate materials because of its favorable specific strength with high melting points and excellent corrosion resistance [1,2]. Despite these attractive properties, Cr has an intrinsic brittleness at room temperature owing to its high ductile-to-brittle transition temperature (DBTT) characteristics, which is similar to other refractory metals such as molybdenum and

tungsten [3]. The high melting point and brittle nature make it difficult to process by conventional manufacturing methods and/or limit the application to simple components only.

In this respect, foreseeing the advent of advanced technologies that could potentially replace traditional manufacturing processes and produce a single component or part with the same economy and efficiency as mass production. Among the approaches, the laser powder bed fusion (L-PBF) process, which is one of the representatives of the metal additive manufacturing process (AM), is an emerging manufacturing process that allows the production of complex, near-net-shape parts at once and offers an opportunity to extend applications because the materials are

joined to create track by track and layer by layer, as opposed to subtractive traditional manufacturing methods [4]. It is suitable for the achievement of shape customization. In addition, the microstructure has a cellular/dendritic solidification structure and simultaneous achievement of suppression of segregation during solidification owing to the ultra-high cooling rate (10^5–10^7 K/s) [5,6]. For anisotropic mechanical behavior, strong crystallographic texture formation can be induced with columnar microstructure [7]. The ultimate goal of the L-PBF process may rely on producing reliable components that achieve sufficient/superior material performance by establishing novel lattice structures and/or microstructures without defects. Indeed, various aerospace lattice structures have been explored to optimize stiffness and strength-to-weight through tailored material distribution and unit cell configuration [8,9]. In bio-metallic materials, suppressing the segregation, reducing Young's modulus by forming strong crystallographic textures, and the enhancement of the yield stress is a topic of interest [10–12]. Furthermore, there is also extensive research into structural materials with the aim of improving overall mechanical properties by creating unique microstructures that are not possible with traditional manufacturing processes [13–15]. It has been demonstrated to be an innovative manufacturing process with considerable competitiveness.

However, the defects from the diverse processing conditions and complex thermal history in the L-PBFed refractory metal component still remained a scientific challenge. Especially, the grain boundary cracking behavior as the main crack initiation mechanism of the refractory metals owing to high DBTT and residual stress of the L-PBF process has been reported [16,17]. Even though it is challenging, there are several studies in the literature to mitigate the cracking on the L-PBF of refractory metals. The DBTT phenomenon in body-centered cubic refractory metals is related to the intrinsic energy barrier which is called the Peierls barrier and is associated with temperature-dependent of screw dislocation motion [18–20]. Additional alloying elements, representatively rhenium, can effectively reduce the barrier energy and facilitate the nucleation/movement of kink-pairs on screw dislocation referred to as the solid-solution-softening phenomenon [16,21]. Thus, the studies on pure refractory metal with additional alloying elements demonstrated the enhancement of intrinsic ductility, thereby attributed to the reduction of cracking during the L-PBF process [22]. The formation of carbon-based complexes also acts to effectively alleviate stress accumulation [16].

On the other hand, without the additional alloying elements for the refractory metals, the optimization of processing parameters such as scan strategy [23,24], substrate preheating [25], laser re-scan [26], and scan length approach [27] can be adopted to control the residual stress. During the L-PBF process, heat transfer and molten metal flow are responsible for the transport of energy and mass. Meantime, the residual stress caused by localized heating and cooling during the L-PBF process causes defects/cracks, hindering the application of this manufacturing process to refractory metals. In order to prevent cracking during the L-PBF process, uniform thermal distribution and a slower cooling rate can be considered for refractory metals. Moreover, it has been reported that the formation of crystallographic texture tailoring grain boundary characteristics to prevent cracking results in the densification of the L-PBFed component [28,29].

According to the various densification approaches described above, previous research attempts were made to apply the L-PBF process to Cr [30–32], which demonstrated that optimization processing parameters with the formation of crystallographic texture not only contribute to increasing the densification but also improve the oxidation resistance. In addition, the hardness sensitively changed depending on the densification, which should be enhanced for utilization as structural applications. Nevertheless, only a few previous studies have focused on the L-PBF process to Cr, investigations still remain limited. Especially, the effects of the combination with the preheat temperature and scan length variation in the densification, microstructural evolution, and mechanical properties of the L-PBFed Cr components have not yet been

comprehensively addressed. Moreover, the numerical studies on melt pool geometry and thermal history during the L-PBF process provide an enhanced understanding and insights into tuning the densification and microstructure to advance its properties. Therefore, this study has the potential to improve the overall reliability of L-PBFed Cr parts for diverse industrial applications.

2. Materials and methods

2.1. Evaluation of the raw powder characteristics and sample fabrication

An irregular shape of pure Cr powder (>99% purity, JFE Material, Japan) was supplied as a starting material, which is confirmed by using field emission scanning electron microscopy (FE-SEM; JEM-4610F, JEOL, Japan) as shown in Fig. 1(a). The average particle size was measured using a Mastersizer 3000E particle size analyzer (Malvern Panalytical, UK), and the laser absorption of powder was determined using an ultraviolet–visible near-infrared spectrophotometer (V-770, Jasco, Japan). In addition, a rotary-drum-type powder flowability measuring device (Revolution Powder Analyzer, Mercury Scientific, US) was used to measure the rest fractal, avalanche angle. To compare the characteristics of raw powder, the spherical morphology of gas-atomized Ti–6Al–4V alloy powder (Osaka Titanium Technologies, Japan) was also evaluated with the same methodology.

As described in Fig. 1(b), an L-PBF machine (EOS M290, EOS, Germany) equipped with a 400 W Yb-fiber laser as the primary heat source was used to fabricate the samples with dimensions of 10 mm × 10 mm × 5 mm along the x-, y-, and z-axes, respectively. Preheat temperatures of 80 °C and 200 °C were applied. The 80 °C preheat temperature was used to avoid unexpected temperature fluctuations caused by laser energy input during the manufacturing process and to maintain a constant fabrication condition. For the 200 °C preheat temperature, the maximum preheat temperature setting of the equipment used. Furthermore, shorter scan length samples were fabricated in size of 5 mm × 5 mm × 5 mm at a preheat temperature of 200 °C to maximize the heat accumulation effect. A bi-directional scanning with 90° rotation between layers was used to minimize the residual stress [24], and various input energy density (*ED*) conditions were attempted to optimize the process parameters.

2.2. Characterization

The densification of the as-built Cr samples was measured by the Archimedes principle using ethanol at room temperature. The theoretical density of 7.19 g/cm^3 for pure Cr was used to determine the relative density. The specimens were then sectioned on the yz-plane representing the x-scan direction by wire electrical discharge machine (Fig. 1(b)), and prepared as mirror polish surface quality. The relative densities of specimens were additionally evaluated for representative samples using an optical microscope (OM; Eclipse LV-150, Nikon, Japan) and ImageJ software. The phase analysis of the as-built Cr specimens was carried out by X-ray diffraction (XRD, RINT-2500V, Rigaku, Japan) using Cu Kα radiation with a wavelength of 0.154 nm. The XRD data were obtained through point scanning in the 2θ angular range from 30° to 90° with a step size of 0.02° and a scan time of 2 s per step at room temperature. Microstructural characteristics were analyzed using FE-SEM equipped with electron backscatter diffraction (EBSD; NordlysMax^3, Oxford Instruments, UK), and transmission electron microscopy (TEM; JEM-ARM200F, JEOL, Japan). In terms of the mechanical properties evaluation, hardness was assessed using Vickers (HMV-G, Shimadzu, Japan) and nanoindentation (ENT-1100a, ELONIX, Japan) tests. The former test was performed with a test force of 0.2 kgf, while the latter test was carried out using a Berkovich tip at a force of 10 mN. Furthermore, compression tests (AG-X, Shimadzu, Japan) at room temperature were conducted at a nominal strain rate of $1.7 \times 10^{-4} \text{s}^{-1}$ condition employing the rectangular shape of the test samples with dimensions of 2 × 2 × 5
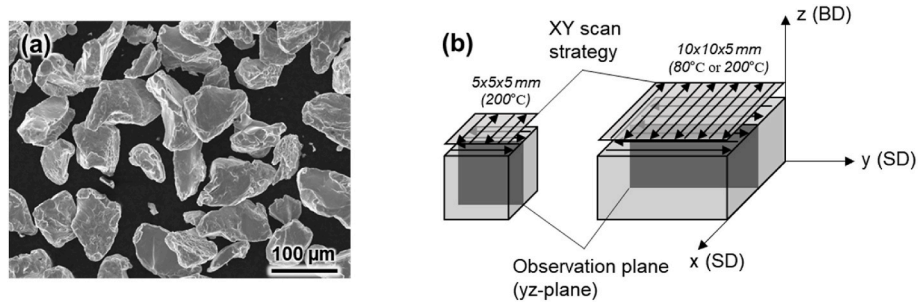
Fig. 1. (a) Irregular shape of pure Cr powder used in the L-PBF process, (b) schematic depiction of the different preheat temperatures with scan lengths, laser scan strategy, and observation plane.

mm. The obtained values were presented as means ± standard deviations.

2.3. Numerical simulations

The laser heat source behavior of multi-scan tracks was estimated by using a finite element thermal model simulation (COMSOL Multiphysics 6.1, COMSOL Inc., Sweden), which uses a Gaussian distribution and the equation can be expressed as follows:

$$Q = \frac{4AP}{\pi R^2 H} \exp\left(-\frac{2r^2}{R^2}\right)\left[1 - \frac{z}{H}\right] \quad (0 < z < H) \tag{1}$$

Where Q is heat per unit volume, P is laser power, R is the radius of the

laser spot, r is the distance from the powder bed surface to the center of the laser spot, A is the laser absorption rate, H is the penetration depth, and z is the depth. To compare the difference in heat accumulation effects taking into account preheat temperature and scan lengths, the different preheat temperatures and model sizes were entered as the same as the L-PBF fabrication conditions above, and the result measurement points were placed in the top surface of the center. The input physical and thermophysical parameters were based on pure Cr, and further detailed methodology can be found in previous studies [13,28].
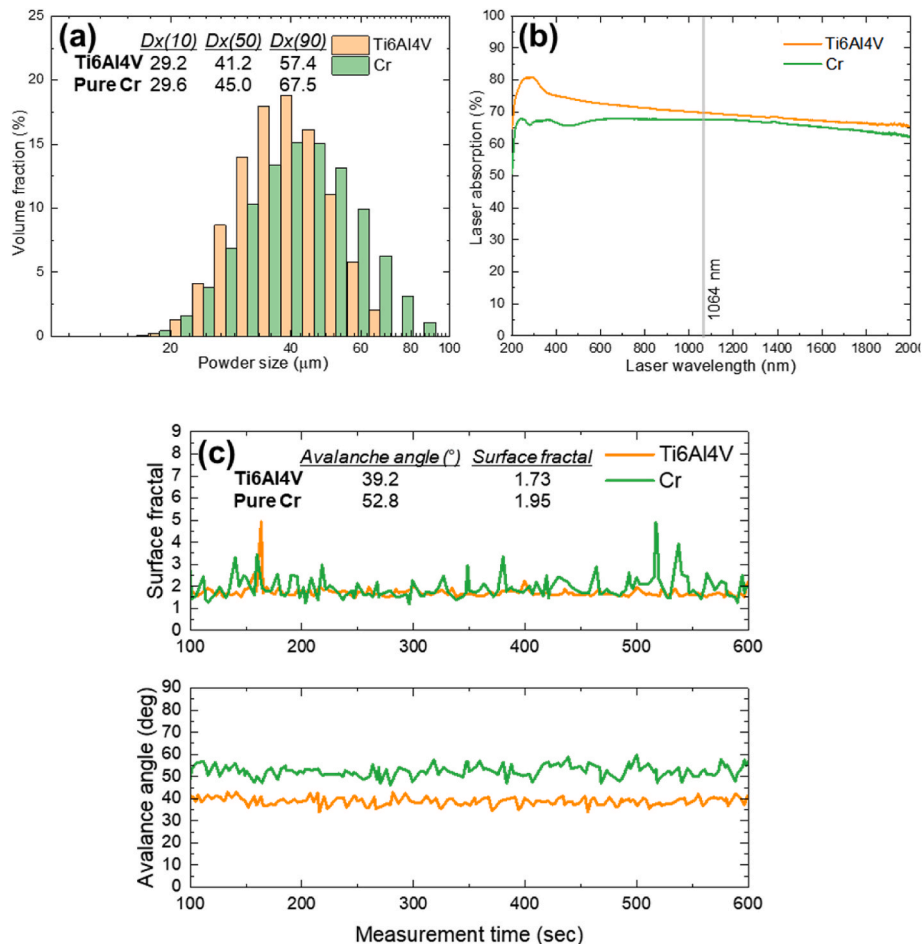

Fig. 2. Comparison of (a) particle size distribution, (b) laser absorption according to the laser wavelength, and (c) flowability of the spherical Ti–6Al–4V and irregular pure Cr powders.

3. Results

3.1. Processability of Cr powder

Fig. 2 displays the comparative characteristics of the spherical Ti–6Al–4V and the irregularly shaped Cr raw powders. The powder size distribution for Ti–6Al–4V and pure Cr were D_{10} = 29.2 μm, D_{50} = 41.2 μm, D_{90} = 57.4 μm, and D_{10} = 29.6 μm, D_{50} = 45.0 μm, and D_{90} = 67.5 μm, respectively (Fig. 2(a)). The laser absorption rate along the laser wavelength shown in Fig. 2(b) demonstrates both types of powders showed relatively high laser absorption at a wavelength of 1064 nm, with Ti–6Al–4V powder (69.78%) performing slightly higher than the pure Cr powder (67.63%). Additionally, the powder flowability is represented by the statistical analysis of the measured avalanche angle and surface fractal (Fig. 2(c)), compared to the Ti–6Al–4V powder, the avalanche angle and surface fractal of pure Cr increased from 39.2° to 52.8° and 1.73 to 1.95, indicating a noticeable decrease in flowability but acceptable powder bed surface quality. The irregular shape of powder is mainly associated with decreasing laser absorption efficiencies owing to low powder bed density resulting from interrupted powder flowability, which is potentially detrimental to the densification of the final product [29]. However, the adoption of non-spherical powder as a feedstock in the powder bed AM processes has been broadly considered to reduce powder production costs [33,34]. Indeed, previous studies demonstrated successful fabrication with favorable structural integrity using the non-spherical powder [30,31], which indicated that the obtained powder characteristics of the irregular shape of pure Cr powder are still appropriate for the L-PBF process.

3.2. Densification of Cr depending on variation in L-PBF process parameters

Fig. 3 depicts the bulk relative density–ED process map measured by the Archimedes principle for the different preheat temperature and scan length variations. A common upward trend of relative density can be found in the 10 mm scan length (feature size 10 x 10 × 5 mm) with 80 °C and 200 °C preheat temperature fabrication groups with the increasing ED. Compared to the 80 °C condition, the most of bulk relative density for the 200 °C preheat temperature was slightly enhanced. On the other hand, the 5 mm scan length (feature size 5 x 5 × 5 mm) with 200 °C condition group resulted in a significant increase of the overall bulk relative density, which gradually increased until ED of 6.25 J/mm^2 and
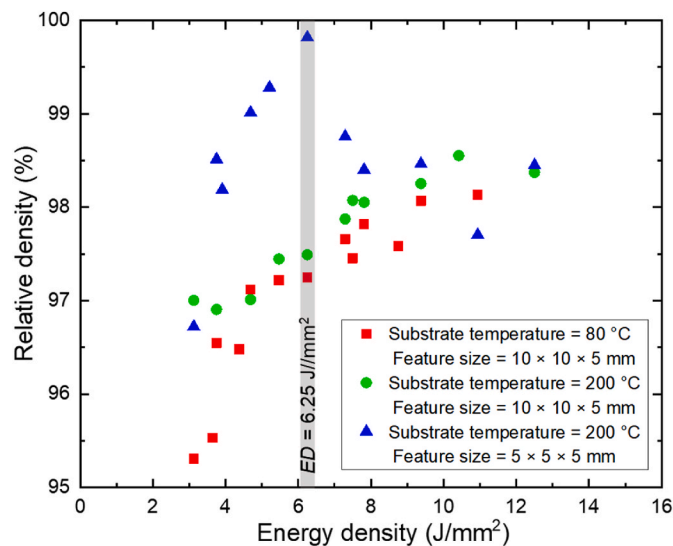
introduced as the optimum condition, while excessively high ED inputs caused a deteriorating in the relative density again, and that is the similar findings in the correlation between various input L-PBF parameters and sample densification [35,36].

In order to discuss solely the effect of the preheat temperature and scan length on optimal densification, the ED of 6.25 J/mm^2 was chosen as the representative sample for each fabrication condition because it includes the highest relative density by the Archimedes principle, which is also similar optimized process parameter condition with our previous studies [31,32]. The detailed applied process parameters for the observation samples included a fixed laser power (P) of 300 W, scan speed (v) of 600 mm/s, layer thickness (h) of 20 μm, and hatch spacing (d) of 80 μm. The corresponding ED input was calculated by Equation (2):

$$ED = \frac{P}{vd} \qquad (2)$$

Moreover, the following abbreviations of the representative samples used in this study are decided according to preheat temperature and scan length conditions. Hereinafter referred to as T80-Cr10, T200-Cr10, and T200-Cr5, respectively.

The densification of the representative samples was simultaneously determined by Archimedes principle and optical relative density (Table 1). At first, the determined bulk relative density, measured by Archimedes principle, the T80-Cr10, T200-Cr10, and T200-Cr5, were 97.2%, 97.5%, and 99.8%, respectively. On the other hand, as shown in Fig. 4(a)–(c), the additional OM images for the representative samples reveal that cracks and residual void defects in the cross-section of the y-z plane were the main distributions hindering full densification. More importantly, the long and curved shape of the cracks was gradually changed to shorter and smaller tortuous when increasing preheat temperature and/or reducing scan length, exhibiting that the crack initiation is effectively suppressed in the same ED condition. Herein, the assessed optical relative density (100% − defects density) for T80-Cr10, T200-Cr10, and T200-Cr5 samples was 97.4%, 97.8%, and 99.2% respectively. There was a slight discrepancy between bulk and optical relative density depending on the measuring methodology because the Archimedes principle difficult to detect interior defects, corresponding to findings in the other studies [17,31].

3.3. Numerical simulation on the effect of preheat and scan length

When the applied preheat temperature and scan length are changed during the sample fabrication, the associated thermal histories are altered. The detailed thermal history variations resulting from the differences in preheat temperature and scan length were plotted in Fig. 5. The obtained results were measured at the midpoint of the 5th scan tracks and the top surface of the center in the simulation model. The

Fig. 3. Bulk relative density–ED plot measured by Archimedes principle for different preheat temperature and scan length variations groups.

Table 1
The representative Cr samples fabricated by the L-PBF process with the corresponding abbreviation, Archimedes relative density, and optical relative density.

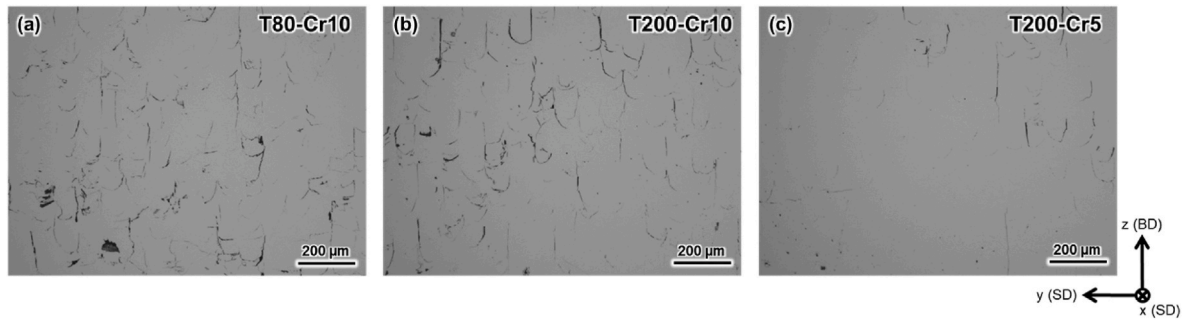| Process parameters (Temperature, energy density, and scan length)	Abbreviation	Archimedes relative density	Optical relative density
80°C 6.25 J/mm^2, x = 10 mm, y = 10 mm, z = 5 mm,	T80-Cr10	97.2%	97.4%
200°C 6.25 J/mm^2, x = 10 mm, y = 10 mm, z = 5 mm	T200-Cr10	97.5%	97.8%
200°C 6.25 J/mm^2, x = 5 mm, y = 5 mm, z = 5 mm	T200-Cr5	99.8%	99.2%

Fig. 4. OM images were obtained from specimens in the y-z plane with (a) T80-Cr10, (b) T200-Cr10, and (c) T200-Cr5 conditions, respectively.
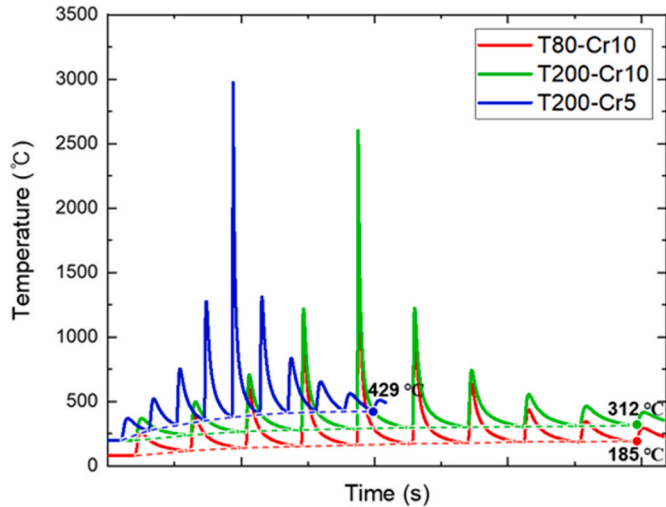

Fig. 5. The corresponding numerical simulated temperature history and time plots of multiple scan tracks.

maximum temperature peaks exceed at least 2500 °C under direct irradiation with a laser heat source revealing that enough energy was provided to produce melt pools in all conditions, and the peaks of T80-Cr10 and T200-Cr200 conditions represented timewisely double times compared to T200-Cr5 because of the scan length. In addition, the different thermal histories can be observed because of the disparity in heat accumulation effects from the adjacent scan tracks. Especially, the peak and valley temperature trend lines (dashed lines) in ascending order are T80-Cr10 < T200-Cr200 < T200-Cr5 in the low-temperature region, and the temperature reached up to 185 °C, 312 °C, and 429 °C when the ten times multi-laser scan tracks were irradiated, respectively.

Fig. 6(a)–(c) shows numerically simulated temperature distribution outcomes of moving scanning tracks for the T80-Cr10, T200-Cr10, and T200-Cr5 samples under yz-, and xy-planes, respectively. Herein, the range from red to yellow colors indicates the above temperature of the melting point of the pure Cr (1863 °C, [1]), thus, which region represented the melt pool geometries during the scan track moving. Noticeably, it can be seen that as the preheat temperature increased and the scan length decreased, the melt pool geometry gradually deepened and elongated. Furthermore, following the regions influenced by the scanning tracks also extending order in T80-Cr10 < T200-Cr10 < T200-Cr5, the T200-Cr5 conditions exhibited relatively long tails compared to others. This implies that the variation of the melt pool geometries and temperature distribution owing to heat accumulation induced by
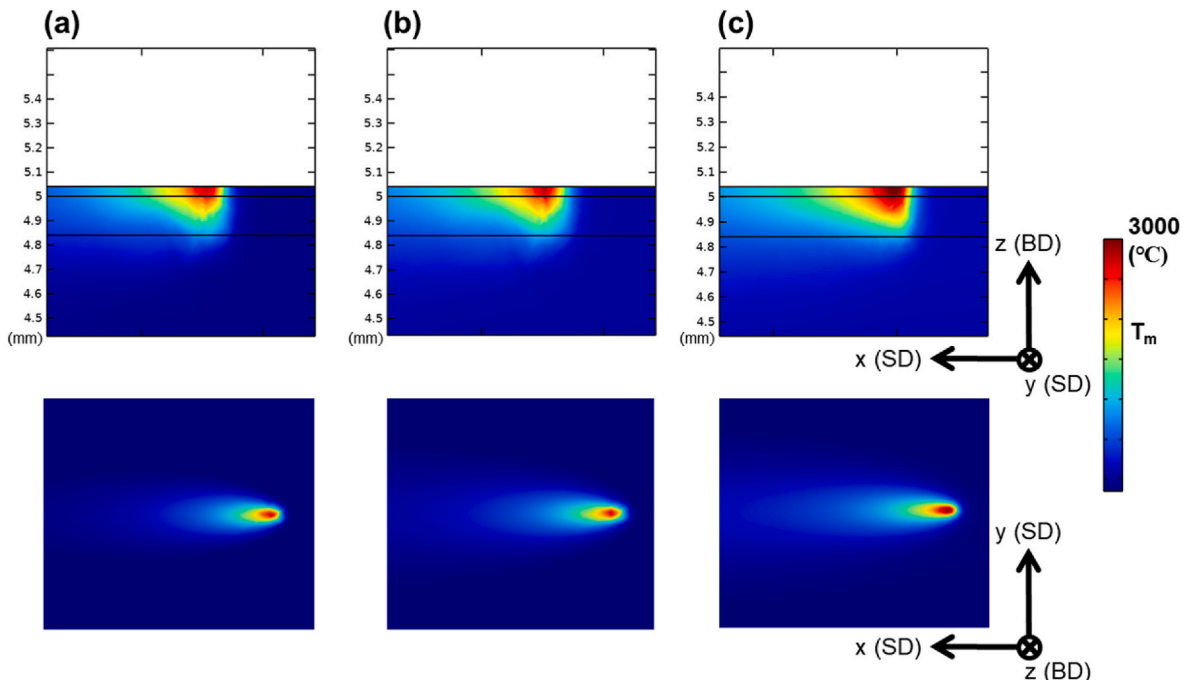

Fig. 6. Comparison of numerical simulated temperature distributions in yz- and xy-plane for (a) T80-Cr10, (b) T200-Cr10, and (c) T200-Cr5 conditions.

differences in preheat temperature and scan length a close correlation to the previously observed densification of samples (Fig. 4).

3.4. Phase and microstructural characteristics

The phase, with respect to different melt pool geometries and temperature distributions resulting from the difference in thermal history depending on the processing parameters, was characterized. For the T80–200, T200-Cr10, and T200-Cr5 conditions, the XRD results confirmed that the fabricated Pure Cr specimens exhibited a single body-centered cubic (BCC) structure, without additional phases (Fig. 7). In addition, to quantitatively evaluate the degree of (100) alignment in the as-built Cr samples, the Lotgering factor, $L(100)$, has been determined from the XRD peak profile with following equation [30,37].

$$L(100) = \frac{A(h00) - B(h00)}{1 - B(h00)} \tag{3}$$

where $A(h00)$, and $B(h00) = \dfrac{\sum Int(h00)}{\sum Int(hkl)}$ $\tag{4}$

In Eqs. (3) and (4), A($h00$) is a ratio of the XRD intensity for the ($h00$) reflection to the sum of the reflections in a scanned range obtained from the as-built Cr specimens, and B($h00$) is an equivalent value for randomly oriented Cr, according to the International Center for Diffraction Data. A larger factor value indicates a stronger texture development in the samples. The evaluated L(100) values were 0.27, 0.31, and 0.43 for the T80–200, T200-Cr10, and T200-Cr5 conditions, respectively.

Furthermore, the inverse pole figure (IPF) maps were colorized according to the crystallographic texture in the yz-plane, and the corresponding {100} pole figures (PFs), high-angle grain boundaries (HAGBs), kernel average misorientation (KAM), Taylor factor maps represent. In the IPF map (Fig. 8(a1–c1)), the various color patterns turn to the red color which indicates the (100) orientation gradually became prominent as the function of preheat temperature increased and the scan length decreased. PFs further corroborate these findings (Fig. 8(a2–c2)), the T80-Cr10 exhibited the lowest multiple of uniform density (MUD) value as 5.55 and the (100) alignment along the y-direction, while the crystal plane rotated between the x-and z-direction. The formation of the crystallographic texture gradually stabilized with the MUD 7.43 at T200-Cr10 and reached the highest MUD 10.03 at the T200-Cr5 condition, which is a corresponding finding with the previously calculated L
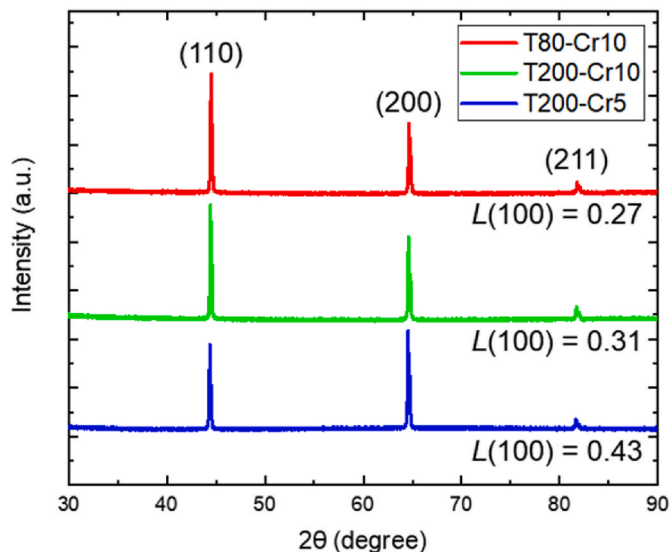
(100) Lotgering factor from XRD data. The crystallographic texture formation caused by the epitaxial growth increased the grain size, therefore, the density of HAGBs (Fig. 8(a3–c3)) is decreased since the strong crystallographic texture is formed. Moreover, stronger texture formation indicates crystal alignment of neighboring grains and a decrease in grain boundary misorientation. Moreover, KAM (Fig. 8 (a4–c4)), which estimates the location involving strain at the microscale [38] and Taylor (Fig. 8(a5–c5)), which is a geometrical indicator of the deformation accommodation efficiency of grains [32,39] decreased with the crystallographic texture strengthening.

Fig. 9 elucidates the distribution of various microstructural characteristics with the quantitative values, including (a) grain size, (b) HAGBs, (c) KAM, and (d) Taylor factor, which provides their correlations. As depicted in Fig. 8(a1–c1, b2–c2), the development of the strong crystallographic texture allows grain elongation and growth across the melt pools and less misoriented HAGBs. Therefore, the average grain size gradually increased from 21.61 μm in the T80-Cr10 condition up to 25.70 μm in the T200-Cr5 condition while the tendency of HAGBs distributions shifted from a higher (45–60°) angle to lower angles (15–30°).

On the other hand, sufficient heat accumulation from the adjacent scan tracks increases the low-temperature region and slows down the cooling rates (Fig. 5). It is attributed to reducing the occurrence of residual stress and/or promoting stress relaxation during the L-PBF process [14,40]. Therefore, the T80-Cr10 sample suffered relatively higher residual stress represented with the average of 1.17° KAM and 2.62 of Taylor factor values, while it gradually decreased until 0.89° of KAM and 2.49 of Taylor factor in the T200-Cr5 benefited according to the relatively higher heat accumulation. In addition, all trends of distributions were also well matched with the order of the average values.

Fig. 10(a and b) shows typical TEM images of the T80-Cr10 and T200-Cr5 conditions. There were no clear differences that can be found depending on the processing parameters. Numerous dislocations commonly evolved because of the rapid solidification characteristics of the L-PBF process. In addition, nanoparticles were distributed regardless of the specific location, such as matrix and grain boundaries. Together with its corresponding energy-dispersive X-ray spectrometry (EDS) mapping in the T200Cr-5 condition (Fig. 10(c and d)), it was verified as oxide particles by enrichment of O. However, the Cr concentration in the matrix is higher than the oxide particles, thus, the Cr concentration in the oxide was hardly detected. The quantitative chemical composition of oxide was 91.77 wt.% of Cr and 8.23 wt.% of O, while the matrix was 98.72 wt.% of Cr and 1.28 wt.% of O by the TEM-EDS point analysis, respectively. These results imply that even though the L-PBF process was executed under the high-purity Ar gas atmosphere, still the 100 ppm below oxygen content exists, which makes the formation of the compound. To reduce the oxide particles, process parameters of the L-PBF process such as input energy density, shield gas flow, scanning strategies, and fabrication atmosphere should be considered with the purity of starting materials. Low oxygen content was found in the samples with higher input energy and shield gas flow rate, opposite and perpendicular scanning direction to the shielding gas flow, and Ar atmosphere [41,42].

3.5. Mechanical properties

The mechanical properties of differently fabricated Cr samples were evaluated (Fig. 11(a–d)). The nano hardness of the T80-Cr10, T200-Cr10, and T200-Cr5 were 3.77 ± 0.25, 3.11 ± 0.07, and 2.82 ± 0.12 GPa, respectively. It was higher values manifested than compared to other studies [19,43], possible reasons for the increasing nano hardness can be considered to be the aforementioned residual stress because of the rapid solidification of the L-PBF process, and containing interstitials such as O [1,44]. Furthermore, the Vickers hardness also similarly exhibited a descending order when the preheat temperature increased and the scan length decreased. The T80-Cr10 samples represented the highest hardness value of 251.1 ± 7.1 HV. While T200-Cr10 showed 221.2 ± 5.6 HV, and T200-Cr5 was 200.6 ± 9.5 HV, which is the lowest.

Fig. 7. Typical XRD patterns of the T80-Cr10 T200-Cr10, and T200-Cr5 conditions with individual Lotgering factors.
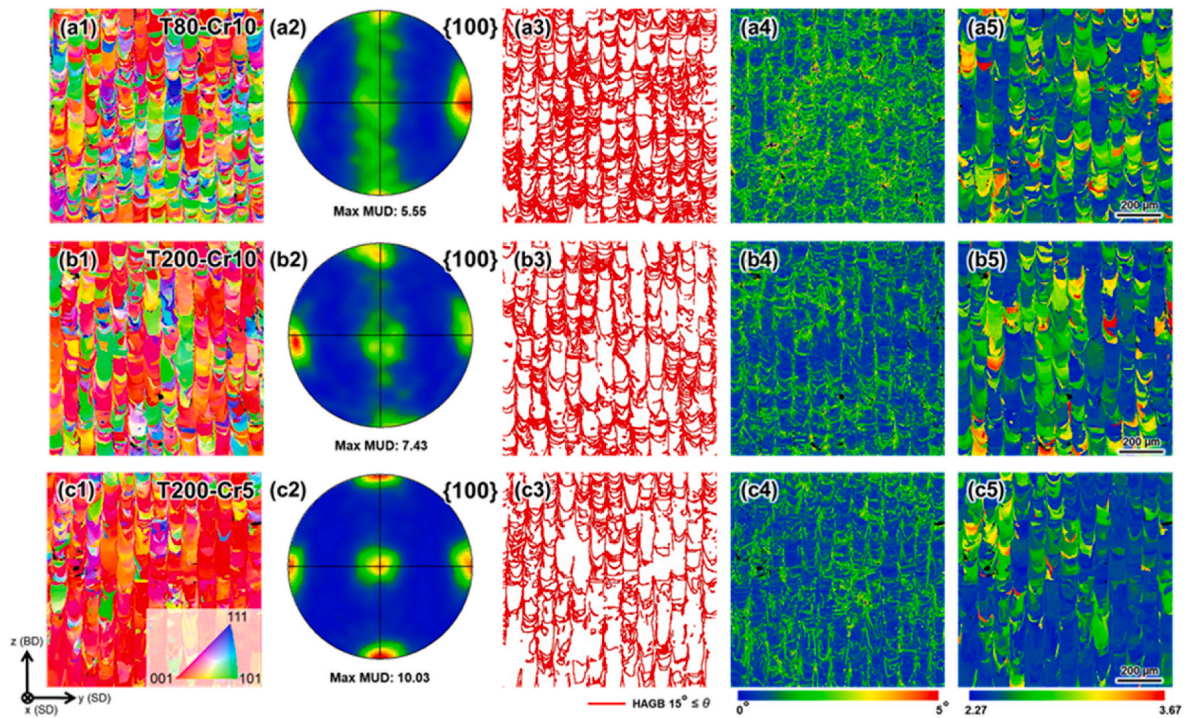
Fig. 8. (a1–c1) IPF maps and (a2–c2) {100} PFs for the yz-plane for the T80-Cr10, T200-Cr10, and T200-Cr5 conditions. Corresponding (a3–c3) HAGBs, (a4–b4) KAM, and (a5–c5) Taylor factor maps, respectively.
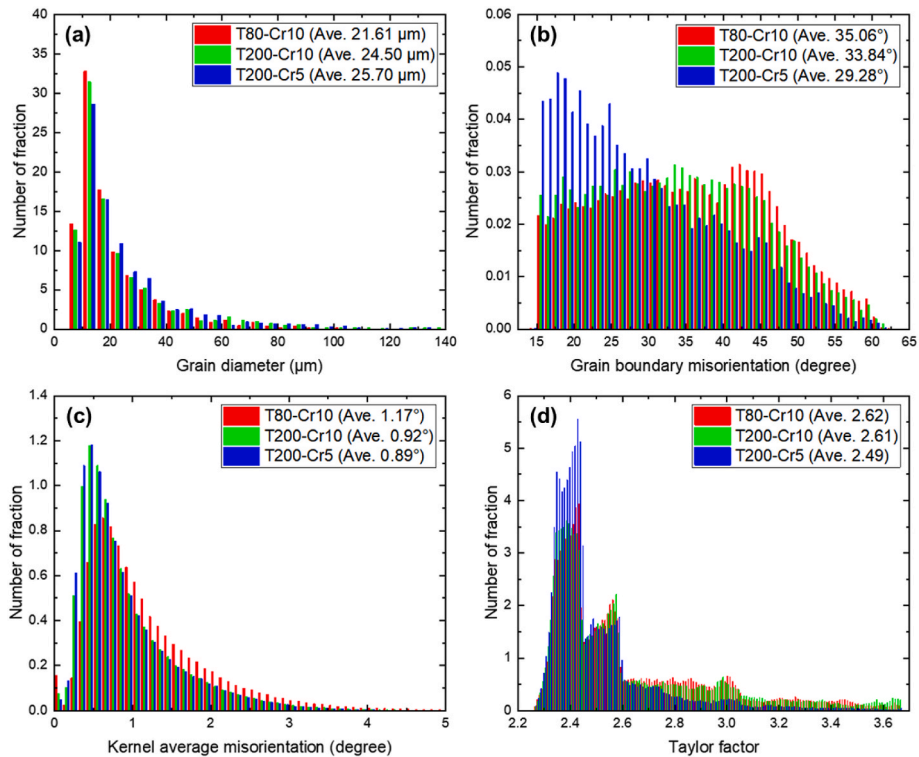

Fig. 9. Distribution of (a) grain size, (b) HAGBs, (c) KAM, and (d) Taylor factor with the quantitative average values for T80-Cr10, T200-Cr10, and T200-Cr5 conditions.

On the other hand, the evaluated compressive yield strength (CYS) and the ultimate compressive strength (UCS) for the T80-Cr10 and T200-Cr10 conditions were 453.1 ± 31.8 MPa, 731.1 ± 41.1 MPa, and 412.5 ± 24.2 MPa, 688.7 ± 19.2 MPa. It had a positive correlation with the hardness test. Additionally, the corresponding compressive strain

(CS) was $11.5 \pm 0.8\%$ and $14.2 \pm 0.7\%$ because the trade-off between the strength and ductility of materials and the increased densification contributed to the resistance for the early fracture during the compression tests. However, the CYS, UCS, and CS of T200-Cr5 indicated 357.7 ± 31.5 MPa, 768.1 ± 29.0 MPa, $19.6 \pm 1.5\%$, respectively. Although the
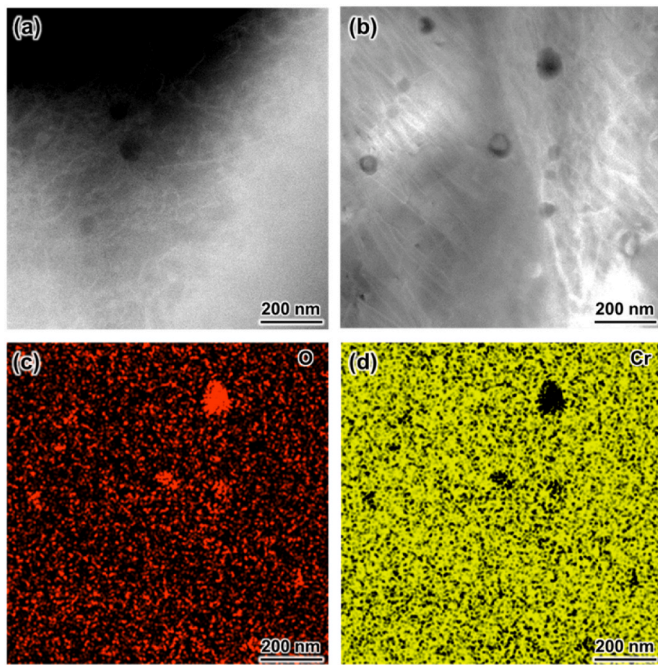
Fig. 10. TEM images of the (a) T80-Cr10 and (b) T200-Cr5 conditions and corresponding elemental mapping images of (b) T200-Cr5 for (c) O and (d) Cr.

CYS was the lowest, the highest UCS and CS values were represented. The mechanical properties of differently fabricated Cr samples are summarized in Table 2.

Fig. 12 shows the deformed T80-Cr10 and T200-Cr5 samples, representing the lowest and highest CS among the compression test results. While T80-Cr10 showed straight cracks with no visible deformation on grains, T200-Cr5 exhibited deformed grains. It was difficult to find slip

lines in the T80-Cr10 condition, while the occurrence of single and multiple slip lines was visible in the T200-Cr5 condition.

4. Discussion

4.1. The effect of thermal history on densification

To understand the key factors for the origin of densification depending on the processing parameters by priority, an investigation of the T200-Cr5 sample with less cracking was conducted using SEM-EBSD. As a result, it was found that cracks were mainly initiated and propagated at the grain boundaries of differently-oriented grains (Fig. 13(a and b)). The detailed line 1 and 2 profiles near the crack had high misorientation angles such as 32° and 31°, while the crack-free regions had a low misorientation angle of less than 15° due to the epitaxial growth (Fig. 13(c)). Furthermore, as shown in (Fig. 13(d–f), the corresponding distribution of HAGBs was well-matched with the KAM, which estimates the extent of deformation or strain because it is the result of the calculation of the average misorientation between a point on the grid and its neighbors [38], and the Taylor factor maps, which describe the susceptibility to deformation of grains [32,39]. Therefore, cracks tended to propagate along the HAGBs, which reflects high-stress concentration regions due to the deformation of grains. Such grain boundary cracking

Table 2

Summarized mechanical properties of T80-Cr10, T200-Cr10, and T200-Cr5 samples.

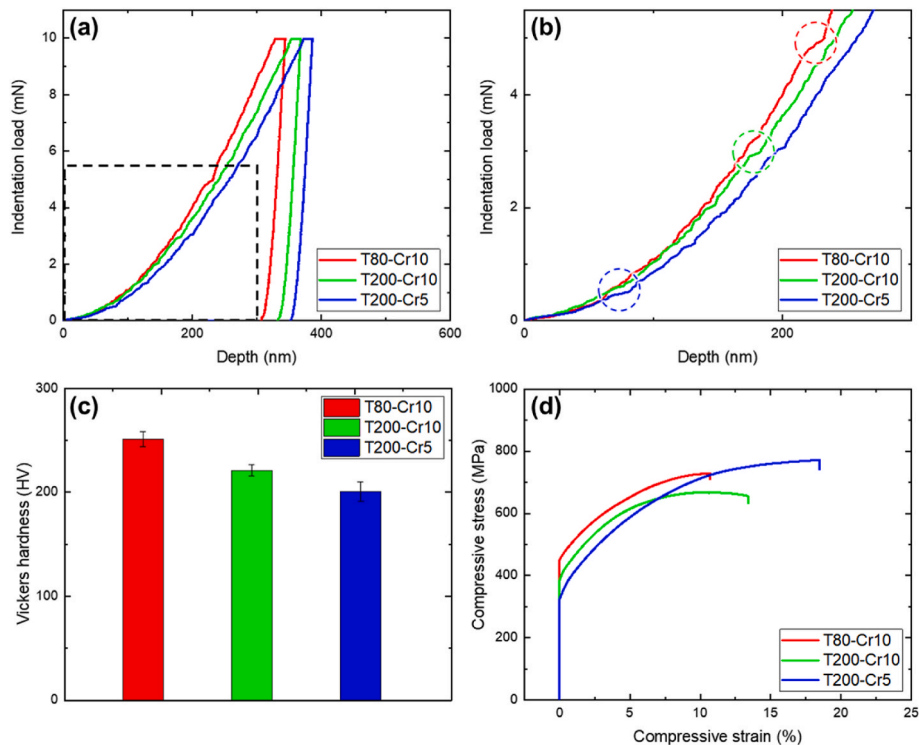| Mechanical properties	T80-Cr10	T200-Cr10	T200-Cr5
Nano hardness (GPa)	3.77 ± 0.25	3.11 ± 0.07	2.82 ± 0.12
Vickers hardness (HV 0.2)	251.1 ± 7.1	221.2 ± 5.6	200.6 ± 9.5
Compressive yield strength (MPa)	453.1 ± 31.8	412.5 ± 24.2	357.7 ± 31.5
Ultimate compressive strength (MPa)	731.1 ± 41.1	688.7 ± 19.2	768.1 ± 29.0
Compressive strain (%)	11.5 ± 0.8	14.2 ± 0.7	19.6 ± 1.5

Fig. 11. (a) a representative *P–h* curves of nano hardness tests, (b) is an enlarged image in (a) as black dashed lines, (c) Vickers hardness, and (d) room temperature compressive properties of T80-Cr10, T200-Cr10, and T200-Cr5 conditions.
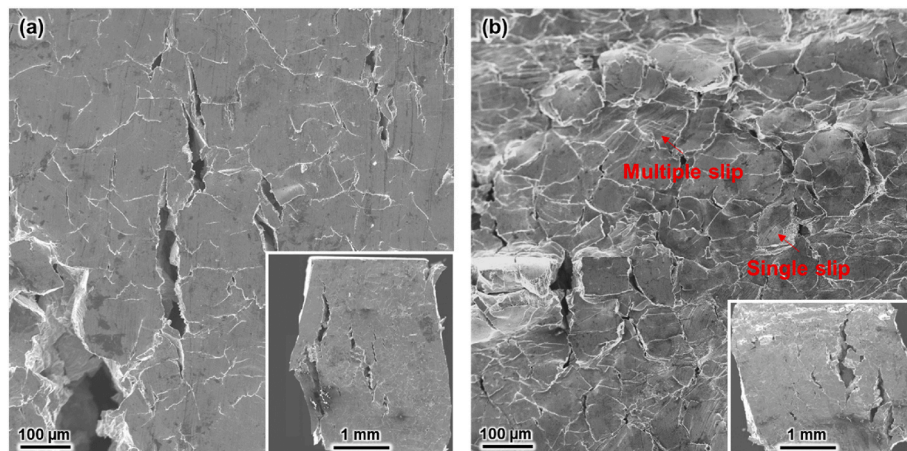
Fig. 12. Typical surface deformation morphologies of T80-Cr10 and T200-Cr5 conditions.
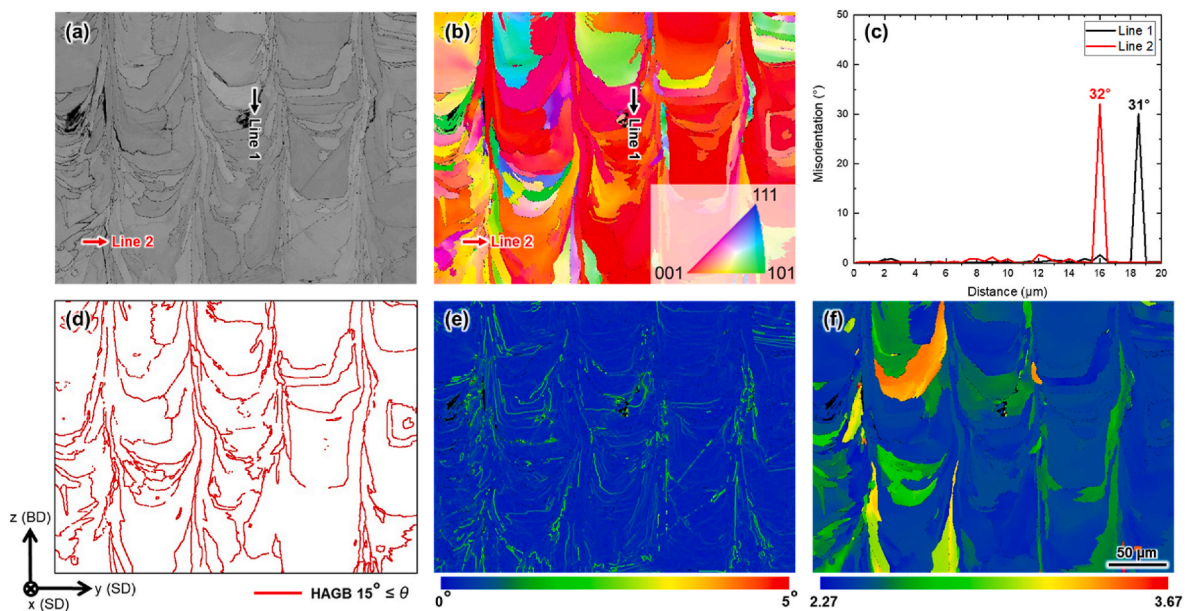

Fig. 13. (a) Band contrast image and (b) IPF map observed from T200-Cr5 sample. (c) misorientation angle of adjacent grains along lines 1 and 2 indicated in (a) and (b). (d–f) The corresponding HAGB, KAM, and Taylor factor maps, respectively.

is frequently observed in the L-PBFed refractory BCC metals resulting from the high residual stress during the manufacturing process and the nature of DBTT characteristics [16,17,22].

Since the preheat temperature increased and scan length decreased at the input *ED* 6.25 J/mm^2, the relative density of the L-PBFed Cr showed a favorable trend (Figs. 3 and 4). This highlights the current densification behavior influenced by melt pool geometry and temperature distributions resulting from the different thermal history depending on the processing parameters (Figs. 5 and 6). Furthermore, it can be deduced that the reducing residual stress and HAGBs is effective for decreasing the magnitude of the cracking in the L-PBFed Cr samples (Fig. 13). Firstly, the cooling rate of the L-PBF process has been estimated to be 10^5–10^7 K/s, which is at least several orders of magnitude faster than that of other typical manufacturing processes such as casting. In addition, the subsequent melting and cooling during the complex thermal histories of the L-PBF process creates significant thermal gradients resulting in the generation of large residual stress, which can cause severe deformation and failure with fabricating samples. As a result, cracks have occurred within L-PBFed Cr samples, which should be controlled to increase the densification. In fact, according to the

numerically simulated thermal history, the higher preheat temperature and shorter scan length were effective in heat accumulation (Fig. 5), demonstrating a positive effect on the relaxation of the residual stress and increasing densification (Fig. 4). It can be explained by the influence of the heat accumulation on slowing down the cooling rate and decreasing the thermal gradient between the melted regions and surroundings, eventually decreasing the level of the residual stress during the L-PBF process [26,45], moreover, keeping the temperature higher than the DBTT of materials during the fabrication is the safest way to prevent cracking and achieve high densification.

On the one hand, the deepened and elongated melt pool geometry owing to the effect of heat accumulation promoted the formation of strong crystallographic texture and optimized the grain boundary characteristics, which were highly effective for increasing densification. The transition from weak to strong (100) cubic texture is related to constitutional supercooling, which is determined by the ratio of the thermal gradient (*G*) and the migration velocity of the solid-liquid interface (*R*) [30,46]. Increasing the *G/R* ratio tends to produce a columnar microstructure in which epitaxial growth is possible while decreasing the *G/R* tends to produce an equiaxed microstructure due to

increased supercooling [13,47]. It has been reported that *R* increases with a decrease in the laser power or an increase in the scanning speed [46], which implies a decrease in the laser energy density resulting in increasing *R* [48], thus, inhibiting the epitaxial growth and opposite case promote strong crystalligraphic texture formation. Although the input *ED* was fixed with 6.25 J/mm^2 in this study, the deepened and elongated melt pool geometry according to the increasing preheat temperature and decreasing scan length can be considered as a similar effect with the increasing total input energy density. Therefore, the strong (100) crystallographic texture formation is presumable, including sufficiently melt pool overlap regions supported grains with <100> alignments and prevention of the sudden loss of the epitaxial growth [49,50]. Meanwhile, the strong crystallographic texture formation resulted in a decrease in the HAGBs densities, and the distribution was predominantly shifted to the lower angle misorientations regions (Figs. 8 and 9). Therefore, the existence of fewer grain boundaries with low misorientation with bigger grain size owing to epitaxial growth indicated less obstacle to dislocation motions induced by residual stress/deformation, which were also represented as lower KAM values and Taylor factors. Eventually, reducing the HAGBs by the formation of a strong crystallographic texture can reduce stress concentration at grain boundaries and suppress the cracks, contributing to the enhancement of the densification, which corresponds findings of L-PBFed W [29].

4.2. The effect of microstructural variation on mechanical properties of L-PBF-ed Cr

As evaluated in Fig. 11, the different thermal histories experienced depending on the processing parameters during the L-PBF process lead to the variation of mechanical properties. In terms of the gradually decreasing tendency of the nano and Vickers hardness with higher preheat temperature and shorter scan length, well aligns with the microstructural variation regardless of crack distribution. The microstructure in the T80-Cr10 condition was characterized by the weakest crystallographic texture development (max MUD 5.55), smallest grain size (Ave. 21.61 μm), and highest HAGBs (Ave. 35.06°) distribution, respectively. These factors are attributed to increasing the hardness and strengths compared to other conditions with regard to the Hall-Petch equation. The grain refinement causes dislocations to pile up at grain boundaries, thereby increasing the stress required to transfer dislocations to neighboring grains [51,52]. In addition, the highest residual stresses were developed owing to the higher cooling rate and inherent thermal gradient, which is confirmed by KAM maps (Ave. 1.17°) and it has been reported that affects the enhancement of the hardness and strength of the materials [53,54]. Similarly, the Taylor factor indicates the resistance to plastic deformation [54]. Large Taylor factor values indicate in the T80-Cr10 specimen (Ave. 2.62) that deformation requires a large amount of slip to act plastic work, consequently expecting higher hardness [32,39]. Meanwhile, the transition followed from the T200-Cr10 to the T200-Cr5 conditions had an opposite microstructural variation. The weak crystallographic texture development has strengthened (∼ max MUD 10.03), grain size increased (∼Ave. 25.70 μm), and HAGBs misorientation decreased (∼29.28°). In addition, the average KAM and Taylor values were also decreased until 0.89° and 2.49, respectively. Therefore, the hardness is represented as a gradually decreasing tendency with higher preheat temperature and shorter scan length.

On the other hand, the compression test results of the T80-Cr10 and T200-Cr10 conditions had a positive correlation with the hardness test results. Therefore, the highest CYS and UCS were compensated as the lowest CS in the T80-Cr10 condition and the slightly lower CYS and UCS represented the CS enhancement in the T200-Cr10 condition. It can be considered that typical observation of strength and ductility trade-offs in various materials. However, the CYS of the T200-Cr5 condition was the lowest, while the UCS and CS were the highest, which implies that not only the observed microstructural characteristics but also the high

densification contributed to the enhancement of the compressive properties. As illustrated in Fig. 11(a), the indentation load (*P*)-depth (*h*) curves showed a difference in the slope. When the load is a constant value at 10 mN, the *h* of the T80-Cr10 was lowest, but gradually increased and it was the highest in the T200-Cr5. Furthermore, as shown in the enlarged image in Fig. 11(b), the pop-in phenomenon was early observed with the transition from T80-Cr10 to T200-Cr5 specimens (Circles). The pop-in phenomenon corresponds to the first stage of plasticity because the abrupt increase in the penetration depth marks the transition from elastic to plastic behavior during the nanoindentation test [55,56]. Therefore, the higher deformation and ductility can be estimated in the T200-Cr5 specimen. As shown in Fig. 12, the developed microstructural characteristics and relatively low densification in the T80-Cr10 condition difficult to accommodate plastic deformation during the compression tests, indicating that almost no slip lines at the surface of the compression sample. In contrast, the T200-Cr5 samples were relatively favorable for the deformation and exhibited clear single and multi-slip lines at the surface morphology, which corresponds to observation with the previous study [18]. Consequently, the occurrence of sufficient slips and multi-slips provides strong work-hardening effects in the high relative density resistance to premature fracture during the compression test, resulting in the highest toughness in the T200-Cr5 condition.

5. Conclusions

This study highlights the significant influence of preheat temperature and scan length on defects and microstructure of pure Cr in the L-PBF process. Simultaneous investigation with the numerical simulation provided insights into understanding the reasons behind the interior defects formation and microstructural evolution mechanisms. In addition, the correlation between the microstructural variation and mechanical properties was investigated, and the following key findings of this study can be summarized as follows.

1. The employment of higher preheat temperatures and shorter scan lengths promised a gradual increase in relative density. Especially, the combination of the increasing preheat temperature and decreasing scan length effectively mitigated defects, and finally manufactured a component showing a relative density of more than 99%.
2. The cracking behavior is mainly associated with the high residual stress owing to the fast cooling rate of the L-PBF process along the HAGBs. The simultaneous heat accumulation of higher preheat temperature and shorter scan length was effective in relieving residual stress owing to the relatively slow cooling rate and strong crystallographic texture formation reducing the HAGBs, KAM, and Taylor factor.
3. The microstructural characteristics of L-PBFed Cr were well reflected in the hardness variations regardless of densification. However, the higher relative density was important for the compressive properties, which prevented premature fracture and accommodated deformation represented as the highest UCS and CS despite the lowest CYS.

The results obtained demonstrate that heat accumulation strategies have worked effectively to achieve high densification of Cr samples produced by the L-PBF process, which not only improves reliability but also shows the potential for extending the application. However, as a refractory material component, further investigation into a highly dense structure and post-processes is required. In particular, the response of the microstructural evolution and performance of L-PBFed materials after heat treatment or hot isostatic pressing is also of interest [57,58]. These are ongoing research activities and will be published in detail elsewhere.

Author contribution

Sung-Hyun Park: Visualization, Investigation, Formal analysis, Writing – original draft. Ozkan Gokcekaya: Conceptualization, Validation, Methodology, Supervision, Data curation, Writing – review & editing. Tatsuya Nitomakida: Investigation, Writing – review & editing. Takayoshi Nakano: Conceptualization, Writing – review & editing, Supervision, Project administration, Funding acquisition.

Declaration of interests

The authors declare that they have no known competing financial interests or personal relationships that could have appeared to influence the work reported in this paper.

Acknowledgments

References

[1] Holzwarth U, Stamm H. Mechanical and thermomechanical properties of commercially pure chromium and chromium alloys. J Nucl Mater 2002;300(2–3): 167–77.

[2] Terentyev D, Zinovev A, Khvan T, You JH, Van Steenberge N, Zhurkin EE. Irradiation embrittlement in pure chromium and chromium-tungsten alloy in a view of their potential application for fusion plasma facing components. J Nucl Mater 2021;554. https://doi.org/10.1016/j.jnucmat.2021.153086.

[3] Gu Y, Harada H, Ro Y. Chromium and chromium-based alloys: problems and possibilities for high-temperature service. J Occup Med 2004;56:28–33.

[4] Frazier WE. Metal additive manufacturing: a review. J Mater Eng Perform 2014;23: 1917–28. https://doi.org/10.1007/s11665-014-0958-z.

[5] Jia Q, Rometsch P, Kürnsteiner P, Chao Q, Huang A, Weyland M, et al. Selective laser melting of a high strength Al–Mn–Sc alloy: alloy design and strengthening mechanisms. Acta Mater 2019;171:108–18. https://doi.org/10.1016/j.actamat.2019.04.014.

[6] Wang H, Wang L, Cui R, Wang B, Luo L, Su Y. Differences in microstructure and nano-hardness of selective laser melted Inconel 718 single tracks under various melting modes of molten pool. J Mater Res Technol 2020;9:10401–10. https://doi.org/10.1016/j.jmrt.2020.07.029.

[7] Cobbinah PV, Matsunaga S, Yamabe-Mitarai Y. Controlled crystallographic texture orientation in structural materials using the laser powder bed fusion process–a review. Adv Eng Mater 2023;25. https://doi.org/10.1002/adem.202300819.

[8] Khan N, Riccio A. A systematic review of design for additive manufacturing of aerospace lattice structures: current trends and future directions. Prog Aerosp Sci 2024;149. https://doi.org/10.1016/j.paerosci.2024.101021.

[9] Eren Z, Gokcekaya O, Balkan D, Nakano T, Mecitoğlu Z. Comparison of in-plane compression of additively manufactured Ti6Al4V 2D auxetic structures: lattice design, manufacturing speed, and failure mode. Mater Des 2024;241. https://doi.org/10.1016/j.matdes.2024.112885.

[10] Ishimoto T, Hagihara K, Hisamoto K, Sun S-H, Nakano T. Crystallographic texture control of beta-type Ti–15Mo–5Zr–3Al alloy by selective laser melting for the development of novel implants with a biocompatible low Young's modulus. Scr Mater 2017;132:34–8. https://doi.org/10.1016/j.scriptamat.2016.12.038.

[11] Gokcekaya O, Ishimoto T, Nishikawa Y, Kim YS, Matsugaki A, Ozasa R, et al. Novel single crystalline-like non-equiatomic TiZrHfNbTaMo bio-high entropy alloy (BioHEA) developed by laser powder bed fusion. Mater Res Lett 2023;11:274–80. https://doi.org/10.1080/21663831.2022.2147406.

[12] Ishimoto T, Ozasa R, Nakano K, Weinmann M, Schnitter C, Stenzel M, et al. Development of TiNbTaZrMo bio-high entropy alloy (BioHEA) super-solid solution by selective laser melting, and its improved mechanical property and biocompatibility. Scr Mater 2021;194. https://doi.org/10.1016/j.scriptamat.2020.113658.

[13] Gokcekaya O, Ishimoto T, Hibino S, Yasutomi J, Narushima T, Nakano T. Unique crystallographic texture formation in Inconel 718 by laser powder bed fusion and its effect on mechanical anisotropy. Acta Mater 2021;212:116876. https://doi.org/10.1016/j.actamat.2021.116876.

[14] Park SH, Gokcekaya O, Oh MH, Nakano T. Effects of hatch spacing on densification, microstructural and mechanical properties of β-solidifying γ-TiAl alloy fabricated by laser powder bed fusion. Mater Charact 2024;214. https://doi.org/10.1016/j.matchar.2024.114077.

[15] Martin JH, Yahata BD, Hundley JM, Mayer JA, Schaedler TA, Pollock TM. 3D printing of high-strength aluminium alloys. Nature 2017;549:365–9. https://doi.org/10.1038/nature23894.

[16] Chen J, Wang X, Li K, Li M, Fu X, Hu R, et al. A novel performance optimization study in additively manufactured tungsten-5 wt.%Rhenium alloys reinforced with dilute carbon. Scr Mater 2024;240. https://doi.org/10.1016/j.scriptamat.2023.115851.

[17] Sidambe AT, Tian Y, Prangnell PB, Fox P. Effect of processing parameters on the densification, microstructure and crystallographic texture during the laser powder bed fusion of pure tungsten. Int J Refract Metals Hard Mater 2019;78:254–63. https://doi.org/10.1016/j.ijrmhm.2018.10.004.

[18] Lu Y, Han WZ. Lowering the ductile-to-brittle transition temperature to -36 °C via fine-grained structures in chromium. Scr Mater 2024;239. https://doi.org/10.1016/j.scriptamat.2023.115813.

[19] Choi IC, Brandl C, Schwaiger R. Thermally activated dislocation plasticity in body-centered cubic chromium studied by high-temperature nanoindentation. Acta Mater 2017;140:107–15. https://doi.org/10.1016/j.actamat.2017.08.026.

[20] Vitek V. Core structure of screw dislocations in body-centred cubic metals: relation to symmetry and interatomic bonding. Philos Mag A 2004;84:415–28. https://doi.org/10.1080/14786430310001611644.

[21] Hu YJ, Fellinger MR, Bulter BG, Wang Y, Darling KA, Kecskes LJ, et al. Solute-induced solid-solution softening and hardening in bcc tungsten. Acta Mater 2017; 141:304–16. https://doi.org/10.1016/j.actamat.2017.09.019.

[22] Wang D, Wang Z, Li K, Ma J, Liu W, Shen Z. Cracking in laser additively manufactured W: initiation mechanism and a suppression approach by alloying. Mater Des 2019;162:384–93. https://doi.org/10.1016/j.matdes.2018.12.010.

[23] Robinson J, Ashton I, Fox P, Jones E, Sutcliffe C. Determination of the effect of scan strategy on residual stress in laser powder bed fusion additive manufacturing. Addit Manuf 2018;23:13–24. https://doi.org/10.1016/j.addma.2018.07.001.

[24] Cheng B, Shrestha S, Chou K. Stress and deformation evaluations of scanning strategy effect in selective laser melting. Addit Manuf 2016;12:240–51. https://doi.org/10.1016/j.addma.2016.05.007.

[25] Vrancken B, Ganeriwala RK, Martin AA, Matthews MJ. Microcrack mitigation during laser scanning of tungsten via preheating and alloying strategies. Addit Manuf 2021;46. https://doi.org/10.1016/j.addma.2021.102158.

[26] Waqar S, Guo K, Sun J. Evolution of residual stress behavior in selective laser melting (SLM) of 316L stainless steel through preheating and in-situ re-scanning techniques. Opt Laser Technol 2022;149. https://doi.org/10.1016/j.optlastec.2021.107806.

[27] Promoppatum P, Yao SC. Influence of scanning length and energy input on residual stress reduction in metal additive manufacturing: numerical and experimental studies. J Manuf Process 2020;49:247–59. https://doi.org/10.1016/j.jmapro.2019.11.020.

[28] Todo T, Ishimoto T, Gokcekaya O, Oh J, Nakano T. Single crystalline-like crystallographic texture formation of pure tungsten through laser powder bed fusion. Scr Mater 2022;206:114252. https://doi.org/10.1016/j.scriptamat.2021.114252.

[29] Gokcekaya O, Ishimoto T, Todo T, Wang P, Nakano T. Influence of powder characteristics on densification via crystallographic texture formation: pure tungsten prepared by laser powder bed fusion. Addit Manuf Lett 2021;1:100016. https://doi.org/10.1016/j.addlet.2021.100016.

[30] Gokcekaya O, Hayashi N, Ishimoto T, Ueda K, Narushima T, Nakano T. Crystallographic orientation control of pure chromium via laser powder bed fusion and improved high temperature oxidation resistance. Addit Manuf 2020;36: 101624. https://doi.org/10.1016/j.addma.2020.101624.

[31] Gokcekaya O, Ishimoto T, Todo T, Suganuma R, Fukushima R, Narushima T, et al. Effect of scan length on densification and crystallographic texture formation of pure chromium fabricated by laser powder bed fusion. Crystals 2021;11:1–14. https://doi.org/10.3390/cryst11010009.

[32] Kim YS, Gokcekaya O, Matsugaki A, Nakano T. Effect of laser scan speed on defects and texture development of pure chromium metal fabricated via powder bed fusion-laser beam. Materials 2024;17. https://doi.org/10.3390/ma17092097.

[33] Ding W, Chen G, Qin M, He Y, Qu X. Low-cost Ti powders for additive manufacturing treated by fluidized bed. Powder Technol 2019;350:117–22. https://doi.org/10.1016/j.powtec.2019.03.042.

[34] Asherloo M, Wu Z, Sabisch JEC, Ghamarian I, Rollett AD, Mostafaei A. Variant selection in laser powder bed fusion of non-spherical Ti-6Al-4V powder. J Mater Sci Technol 2023;147:56–67. https://doi.org/10.1016/j.jmst.2022.10.045.

[35] Li S, Lan X, Wang Z, Mei S. Microstructure and mechanical properties of Ti-6.5Al-2Zr-Mo-V alloy processed by Laser Powder Bed Fusion and subsequent heat treatments. Addit Manuf 2021;48. https://doi.org/10.1016/j.addma.2021.102382.

[36] Narvan M, Ghasemi A, Fereiduni E, Kendrish S, Elbestawi M. Part deflection and residual stresses in laser powder bed fusion of H13 tool steel. Mater Des 2021;204. https://doi.org/10.1016/j.matdes.2021.109659.

[37] Hagihara K, Nakano T, Suzuki M, Ishimoto T, Suyalatu Sun SH. Successful additive manufacturing of MoSi$_2$ including crystallographic texture and shape control. J Alloys Compd 2017;696:67–72. https://doi.org/10.1016/j.jallcom.2016.11.191.

[38] Zhang X, Chen H, Xu L, Xu J, Ren X, Chen X. Cracking mechanism and susceptibility of laser melting deposited Inconel 738 superalloy. Mater Des 2019; 183. https://doi.org/10.1016/j.matdes.2019.108105.

[39] Liu SY, Li HQ, Qin CX, Zong R, Fang XY. The effect of energy density on texture and mechanical anisotropy in selective laser melted Inconel 718. Mater Des 2020;191. https://doi.org/10.1016/j.matdes.2020.108642.

[40] Li X, Liu Y, Tan C, Zou Y. Porosity formation mechanisms, microstructure evolution and mechanical performance of AlMgScZr alloy fabricated by laser powder bed

fusion: effect of hatch distance. J Manuf Process 2023;94:107–19. https://doi.org/10.1016/j.jmapro.2023.03.047.

[41] Eo DR, Chung SG, Jeon JM, Cho JW. Melt pool oxidation and reduction in powder bed fusion. Addit Manuf 2021;41. https://doi.org/10.1016/j.addma.2021.101982.

[42] Haines MP, Peter NJ, Babu SS, Jägle EA. In-situ synthesis of oxides by reactive process atmospheres during L-PBF of stainless steel. Addit Manuf 2020;33. https://doi.org/10.1016/j.addma.2020.101178.

[43] Maier V, Hohenwarter A, Pippan R, Kiener D. Thermally activated deformation processes in body-centered cubic Cr - how microstructure influences strain-rate sensitivity. Scr Mater 2015;106:42–5. https://doi.org/10.1016/j.scriptamat.2015.05.001.

[44] Briant CL, Kumar KS, Rosenberg N, Tomioka H. The mechanical properties of high purity chromium. Int J Refract Met Hard Mat 2000;18(1):9–11.

[45] Chen C, Xiao Z, Wang Y, Yang X, Zhu H. Prediction study on in-situ reduction of thermal stress using combined laser beams in laser powder bed fusion. Addit Manuf 2021;47. https://doi.org/10.1016/j.addma.2021.102221.

[46] Bontha S, Klingbeil NW, Kobryn PA, Fraser HL. Effects of process variables and size-scale on solidification microstructure in beam-based fabrication of bulky 3D structures. Mater Sci Eng A 2009;513–514:311–8. https://doi.org/10.1016/j.msea.2009.02.019.

[47] Yan F, Xiong W, Faierson EJ. Grain structure control of additively manufactured metallic materials. Materials 2017;10(11):1260.

[48] Promoppatum P, Yao SC, Pistorius PC, Rollett AD. A comprehensive comparison of the analytical and numerical prediction of the thermal history and solidification microstructure of Inconel 718 products made by laser powder-bed fusion. Engineering 2017;3:685–94. https://doi.org/10.1016/J.ENG.2017.05.023.

[49] Rolchigo M, Coleman J, Knapp GL, Plotkowski A. Grain structure and texture selection regimes in metal powder bed fusion. Addit Manuf 2024;81. https://doi.org/10.1016/j.addma.2024.104024.

[50] Biswas P, Ma J. Development of crystallographic misorientation in laser powder bed fusion 316L stainless steel. Addit Manuf 2024;80. https://doi.org/10.1016/j.addma.2023.103951.

[51] Hansen N. Hall-petch relation and boundary strengthening. Scr Mater 2004;51: 801–6. https://doi.org/10.1016/j.scriptamat.2004.06.002.

[52] Xiao X, Terentyev D, Chen Q, Yu L, Chen L, Bakaev A, et al. The depth dependent hardness of bicrystals with dislocation transmission through grain boundaries: a theoretical model. Int J Plast 2017;90:212–30. https://doi.org/10.1016/j.ijplas.2017.01.007.

[53] Wang J, Hong H, Huang A, Yang X, Qian R, Shang C. New insight into the relationship between grain boundaries and hardness in bainitic/martensitic steels from the crystallographic perspective. Mater Lett 2022;308. https://doi.org/10.1016/j.matlet.2021.131105.

[54] Wang YC, Lei LM, Shi L, Wan HY, Liang F, Zhang GP. Scanning strategy dependent tensile properties of selective laser melted GH4169. Mater Sci Eng A 2020;788. https://doi.org/10.1016/j.msea.2020.139616.

[55] Piao Y, Li C, Hu Y, Cui H, Luo X, Geng Y, et al. Nanoindentation induced anisotropy of deformation and damage behaviors of MgF_2 crystals. J Mater Res Technol 2024; 28:4615–25. https://doi.org/10.1016/j.jmrt.2024.01.034.

[56] Saini P, Nag S, Jang J il, Choi IC, Ramamurty U, Narayan RL. A statistical analysis of the second 'pop-in' behaviour of the spherical-tip nanoindentation of Zr-based bulk metallic glasses. Materialia 2023;31. https://doi.org/10.1016/j.mtla.2023.101862.

[57] Deirmina F, Adegoke O, Col M Del, Pellizzari M. Effect of layer thickness, and laser energy density on the recrystallization behavior of additively manufactured Hastelloy X by laser powder bed fusion. Addit Manuf lett 2023;7. https://doi.org/10.1016/j.addlet.2023.100182.

[58] Bulutsuz AG, Gulec B, Gokcekaya O, Gardstam J, Nakano T, Yilmazer H. An investigation over microstructure and HIP processing effects on wear performance of pure chromium parts fabricated by laser powder bed fusion. Int J Refract Met Hard Mater 2024;120. https://doi.org/10.1016/j.ijrmhm.2024.106616.